Supporting Information

Ligand Engineering-Modulated Surface Active Site Number in Pt_1Ag_{14} Nanoclusters to Boost Photocatalytic H_2 Production

Linlin Yu,‡ Yonggang Ren,‡ Yue Han, Along Ma, Shuo Zhang, Linwen Zhang,* and Shuxin Wang*

Key Laboratory of Optic-electric Sensing and Analytical Chemistry for Life Science, MOE, Shandong Key Laboratory of Biochemical Analysis, College of Chemistry and Molecular Engineering, Qingdao University of Science and Technology, Qingdao 266042, P. R. China.

*Corresponding authors. E-mail: shuxin_wang@qust.edu.cn (Shuxin Wang) and linwen_zhang@qust.edu.cn (Linwen Zhang);

‡These authors contributed equally to this work.

Notes: The authors declare no competing financial interest.

Table of Contents

Section 1. Synthesis, Characterization, Photoelectrochemical measurements, Photocatalytic hydrogen evolution, and DFT calculations

Section 2. Supporting Figures

Fig. S9 Packing mode of **Pt_1Ag_{14}-1** in the crystal shown.
Fig. S10 Packing mode of **Pt_1Ag_{14}-2** in the crystal shown.
Fig. S11 Comparison of the molecular symmetry between **Pt_1Ag_{14}-1** and **Pt_1Ag_{14}-2** clusters.
Fig. S12 The change in the distance between the shell Ag and the icosahedral surface Ag.
Fig. S13 Structural comparison and bond length among **Pt_1Ag_{14}-1**, and **Pt_1Ag_{14}-2** NCs.
Fig. S14 TEM image image of TiO_2 nanoparticles.
Fig. S15 TEM and elemental mapping analyses of **Pt_1Ag_{14}-2** and **Pt_1Ag_{14}-2/TiO_2** composites.
Fig. S16 TEM image and size distribution histogram (inset) of the unsupported **Pt_1Ag_{14}-1** NCs.
Fig. S17 Powder XRD patterns of **TiO_2**, **Pt_1Ag_{14}-1/TiO_2, and Pt_1Ag_{14}-2/TiO_2**.
Fig. S18 UV-vis diffuse reflection spectroscopy of **TiO_2**, **Pt_1Ag_{14}-1/TiO_2**, and **Pt_1Ag_{14}-2/TiO_2**.
Fig. S19 Hydrogen generation rates of pristine **TiO_2**, **Pt_1Ag_{14}-1** NCs, **Pt_1Ag_{14}-2** NCs, **Pt_1Ag_{14}-1/TiO_2** and **Pt_1Ag_{14}-2/TiO_2** composite.
Fig. S20 Photocatalytic H_2 production performance of **Pt_1Ag_{14}-2/TiO_2** under alternating light on and off conditions.
Fig. S21 HRTEM images and size distribution histogram of **Pt_1Ag_{14}-2** NCs in **Pt_1Ag_{14}-2/TiO_2** after the photocatalytic reaction.
Fig. S22 Photoluminescence spectra obtained with 365 nm excitation for **TiO_2**, **Pt_1Ag_{14}-1/TiO_2** and **Pt_1Ag_{14}-2/TiO_2**.
Fig. S23 Tauc plots of **TiO_2**, and **Pt_1Ag_{14}-2**.
Fig. S24 Mott-Schottky plots of **TiO_2**, and **Pt_1Ag_{14}-2** frequencies of 5000 Hz.
Fig. S25 XPS spectra of Ti 2p and O 1s for **TiO_2**.
Fig. S26 XPS spectra of Ti 2p, O 1s Ag 3d and Pt 4f for **Pt_1Ag_{14}-2/TiO_2**.
Fig. S27 Schematic of the energy level diagram and the mechanism of photocatalytic H_2 generation under solar irradiation in **Pt_1Ag_{14}-2/TiO_2** photocatalysts.
Fig. S28 Comparison of the atomic models before and after H^+ adsorption.

Section 3. Supporting Table

Table S1 Crystal data and structure refinement for **Pt_1Ag_{14}-2**.

Section 1. Synthesis, Characterization, Photocatalytic measurements, DFT calculations, and References

I. Synthesis

Chemicals: All chemicals were obtained from commercial sources and used as received without additional purification. Chloroplatinic acid hexahydrate ($H_2PtCl_6·6H_2O$, 99% metal basis), silver acetate (CH_3COOAg, 98% metals basis), phenyl mercaptan (PhSH, BTH, 97%), 2-Phenylethylmercaptan ($PhCH_2CH_2SH$, PETH, 97%), Tris(4-methoxyphenyl)phosphine (P(Ph-*p*-OMe)$_3$, TMPP, 98%), sodium borohydride ($NaBH_4$, 98%), methyl alcohol (CH_3OH, MeOH, HPLC grade), ethyl alcohol (CH_3CH_2OH, EtOH, HPLC grade), dichloromethane (CH_2Cl_2, DCM, HPLC grade), Titanium dioxide (TiO_2, P25), sodium sulfate (Na_2SO_4), N, N-dimethylformamide (DMF, 99%) and *n*-hexane (C_6H_{14}, Hex, HPLC grade), were used to carry out the experiments. Before use, all glassware was carefully cleaned with aqua regia (3:1 mixture of HCl and HNO_3 by volume), rinsed extensively with purified water, dried in an oven, and subsequently rinsed with dichloromethane and methanol.

Synthesis of $Pt_1Ag_{14}(TMPP)_7(BT)_6$ (Pt_1Ag_{14}-1) NC: Pt_1Ag_{14}-1 NC was synthesized with minor modifications to the previously reported method.[1] Typically, a mixture of $H_2PtCl_6·6H_2O$ (5 mg, 0.00965 mmol) and CH_3COOAg (24.6 mg, 0.1474 mmol) was dissolved in a solvent system comprising 5 mL CH_3OH and 15 mL CH_2Cl_2 under vigorous stirring. After 5 min of stirring, BTH (10 µL, 0.0949 mmol) and TMPP (134.3 mg, 0.381 mmol) were sequentially added. The reaction mixture became yellow and transparent within 30 min. A freshly prepared aqueous solution of $NaBH_4$ (30 mg, 0.793 mmol in 2 mL H_2O) was then introduced dropwise, resulting in gradual darkening of the solution. The reaction was allowed to proceed for 12 h at room temperature, yielding **Pt_1Ag_{14}-1** NCs with approximately 10% yield (based on silver content). The crude product was purified by three successive CH_3OH washes to remove byproducts. Red, block-shaped crystals were obtained by crystallizing the purified NCs in CH_2Cl_2/CH_3OH (1 : 3) system at 4°C over 3 days.

Synthesis of $Pt_1Ag_{14}(TMPP)_6(PET)_6$ (Pt_1Ag_{14}-2) NC: Pt_1Ag_{14}-2 NC was synthesized following an analogous procedure to **Pt_1Ag_{14}-1**, maintaining identical molar ratios of PETH (equivalent to BTH in the previous synthesis). Red, block-shaped crystals were obtained by crystallizing the purified NCs in CH_2Cl_2/CH_3OH (1 : 3) system at 4°C over 3 days.

Synthesis of Pt_1Ag_{14}-2/TiO_2 and Pt_1Ag_{14}-1/TiO_2: A dispersion of TiO_2 (98 mg in 9 mL DMF) was mixed with a solution of the **Pt_1Ag_{14}-2** cluster (2 mg in 2 mL DMF) under vigorous stirring for 30 minutes. The disappearance of the black color indicated the adsorption of the clusters onto the TiO_2 support. Following centrifugation and removal of the supernatant, the solid material was washed with ethanol and dried under vacuum. **Pt_1Ag_{14}-1/TiO_2** was prepared using an identical procedure and the same cluster-to- TiO_2 mass ratio.

II. Characterization

Ultraviolet-Visible Spectroscopy (UV-vis): UV-vis absorption spectra were acquired using a Shanghai Metash UV-8000 spectrophotometer. For solution-phase measurements, crystalline samples were dissolved in CH_2Cl_2 at appropriate concentrations.

Solid-state diffuse reflectance spectroscopy (UV-Vis DRS): UV-Vis DRS was performed on an Agilent Cary 5000 spectrophotometer equipped with an integrating sphere, using $BaSO_4$ as a reflectance reference. Powder samples of **Pt_1Ag_{14}-1/TiO_2** and **Pt_1Ag_{14}-2/TiO_2** were gently ground and packed into a uniform layer for measurement.

X-ray photoelectron spectroscopy (**XPS**): The XPS and UPS measurements were performed on ESCALAB XI+ configured with a monochromated AlKα (1486.8 eV) 150W X-ray source, 0.5 mm circular spot size, a flood gun to counter charging effects, and the analysis chamber base pressure lower than 1 x 10^{-9} mbar, data were collected with FAT = 20 eV. Samples were mounted on conductive tape, with carbon reference (C 1s = 284.8 eV) applied for energy calibration.

Scanning electron microscope-energy dispersive spectrometer (**SEM-EDS**): SEM-EDS analysis was performed using a JEOL JSM-6700F field-emission scanning electron microscope (**Pt_1Ag_{14}-1**) and a Hitachi Regulus 8100 instrument (**Pt_1Ag_{14}-2**). Crystal samples of **Pt_1Ag_{14}-1** and **Pt_1Ag_{14}-2** were mounted on conductive carbon tape and analyzed at accelerating voltages ranging from 0.1 to 30 kV.

X-ray crystallography: The data collections for single crystal X-ray diffraction (SC-XRD) were carried out on a Bruker D8 Quest at 170 K, using a Mo-Kα radiation (λ = 0.71073 Å). The structures were solved by using the structure solution program ShelXT with the Intrinsic Phasing method in the OLEX2 software.[2,3] Refinements were performed on F^2 anisotropically for all the non-hydrogen atoms by the full-matrix least-squares method using the SHELXL program in Olex2 software. And all the hydrogen atoms were set in geometrically calculated positions and refined isotopically using a riding model. Detailed crystal data for **Pt_1Ag_{14}-2** NC are given in Table S1; the supplementary crystallographic data for this compound have been deposited at the CCDC under number 2463176. These data are provided free of charge by the Cambridge Crystallographic Data Centre.

X-ray diffraction (XRD): XRD patterns were recorded on a Rigaku D/MAX/2500PC diffractometer to characterize the crystal structures of **TiO_2, Pt_1Ag_{14}-1/TiO_2 and Pt_1Ag_{14}-2/TiO_2**. Prior to analysis, all powder samples were ground to ensure flat and uniform surfaces.

Transmission electron microscopy (TEM): TEM and energy-dispersive X-ray spectroscopy (EDS) analyses were performed on a JEOL JEM-F200 microscope operated at 200 kV. The samples were prepared by depositing an ethanol dispersion of the clusters onto carbon-coated copper grids and drying under ambient conditions before analysis.

Photoluminescence (PL) spectroscopy: Steady-state PL spectra were collected with an Ocean Optics QE65000 spectrometer. The powder samples were ground and mounted as a thin layer on a quartz slide. A 365 nm laser was used as the excitation source.

III. Photoelectrochemical measurements

All photoelectrochemical (PEC) measurements were performed using a three-electrode system with an electrochemical workstation (CHI 650E). A 0.2 M Na_2SO_4 aqueous solution (pH = 6.8) served as the electrolyte, and the system was illuminated by a 300 W xenon lamp (X300, Qingdao Solar Scientific Instrument High-tech Co., Ltd., China). The working electrode, reference electrode, and counter electrode were the as-prepared catalyst film on FTO, a saturated Ag/AgCl electrode, and a Pt sheet, respectively. To fabricate the working electrode, 2 mg of the catalyst was ultrasonically dispersed in 1 mL of a water/isopropanol mixture (1:1, V/V) containing 20 μL of Nafion for 60 min to form a homogeneous ink. Subsequently, 50 μL of the ink was drop-cast onto a piece of FTO glass and dried at 60°C.

IV. Photocatalytic hydrogen evolution

Photocatalytic hydrogen evolution reactions were carried out in a sealed 150 mL reactor. Typically, 20 mg of the photocatalyst was dispersed in a mixed solution of 18 mL deionized water and 2 mL methanol via ultrasonication. Methanol was introduced as a sacrificial hole scavenger to consume photogenerated holes. The initial pH of the reaction solution was measured to be 6.72 using a pH meter. Prior to irradiation, high-purity Ar gas was bubbled through the suspension to remove dissolved oxygen and other air components, ensuring an inert atmosphere. The reaction system was then exposed to a 300 W Xe lamp (X300, Qingdao Solar Scientific Instrument High-tech Co., Ltd., China) for photoirradiation, and the temperature was maintained at 25 °C by a circulating cooling water bath. The evolved hydrogen gas was quantified using a gas chromatograph (GC-3900 Plus, RUINENG, China).

V. DFT calculations

Computational method

All the calculations were accomplished by the QUICKSTEP module of the CP2K 2024.1, using a hybrid Gaussian and plane-wave (GPW) approach combined with the Perdew-Burke-Ernzerh of (PBE) functional. The pseudopotentials basis set of DZVP-MOLOPT-GTH was employed to described both non-metal atoms and metal atoms. DFT-D3(BJ) was used to describe the dispersion interactions among all the atoms in models. The cutoffs of the four grids were determined by the kinetic energy cut-off of the plane wave basis of 500 Ry. A relative cut-off of 55 Ry that determined the four grids of a given Gaussian function should be mapped. The input files for performing CP2K calculations were generated by Multiwfn software.[4] A geometry optimization was completed when Convergence was smaller than 10^{-6} eV.

The Gibbs free energy for all planes was defined as follows:

$$\Delta G = \Delta E_{*H} + \Delta ZPE - T\Delta S \qquad (2)$$

$$E_{*H} = E_{*H/slab} - E_{*H} - E_{slab} \qquad (3)$$

where ΔE_{*H}, ΔZPE, T, and ΔS are the adsorption energy, zero-point energy difference, temperature, and entropy difference between adsorbed states and gas phases, respectively.

VI. References

1. T. Liu, Y. Li, Y. Zuo, A. Ma, Y. Wang, S. Zhang, X. Ma, Z. Yin, J. Yang and S. Wang, *Nanoscale*, 2025, **17**, 10886-10891.
2. G. M. Sheldrick, *Acta Crystallogr C*, 2015, **71**, 3-8.
3. O. Dolomanov, L. Bourhis, R. Gildea, J. Howard and H. Puschmann, *J. Appl. Cryst. J. Appl. Cryst*, 2009, **42**, 339-341.
4. T. Lu, F. Chen, *J. Comput. Chem.* 2012, **33**, 580-592.

Section 2. Supporting Figures

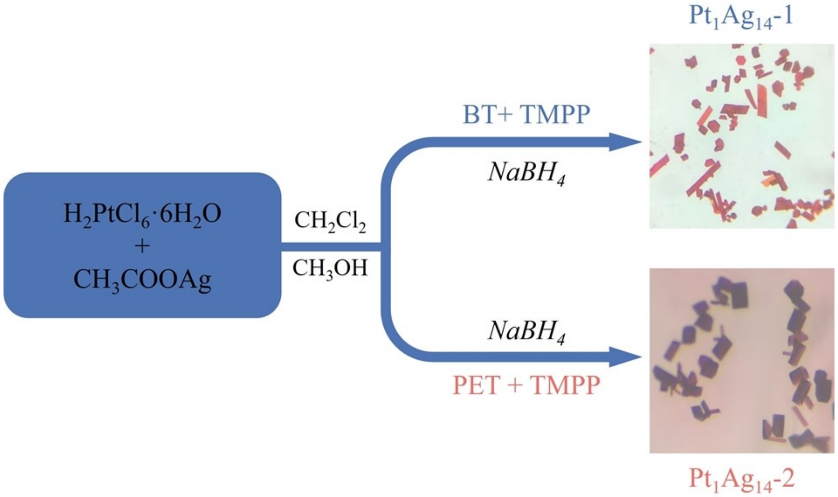

Fig. S1 Synthesis and Crystallization of **Pt_1Ag_{14}-1** and **Pt_1Ag_{14}-2.**

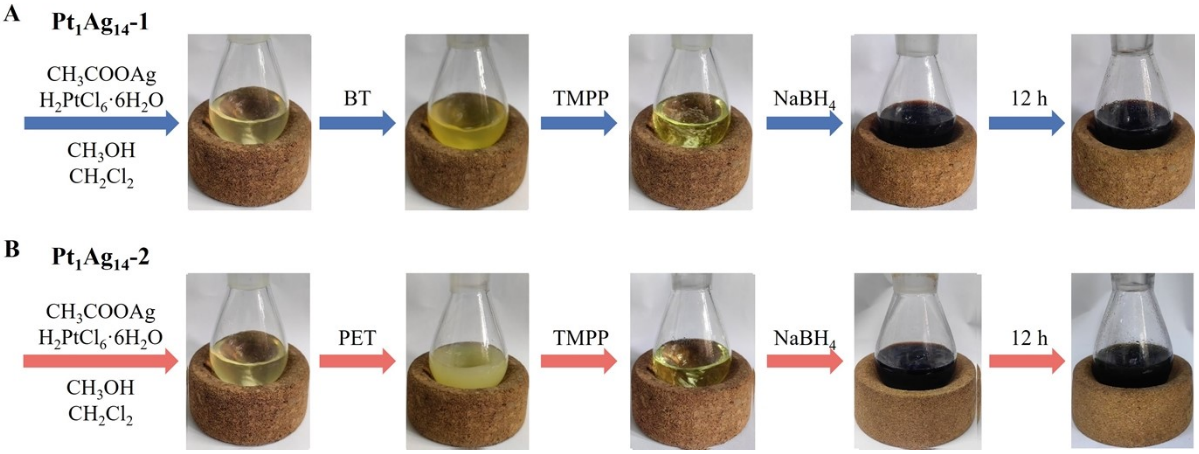

Fig. S2 Experimental phenomenon monitoring during the cluster synthesis process of **Pt_1Ag_{14}-1** and **Pt_1Ag_{14}-2**.

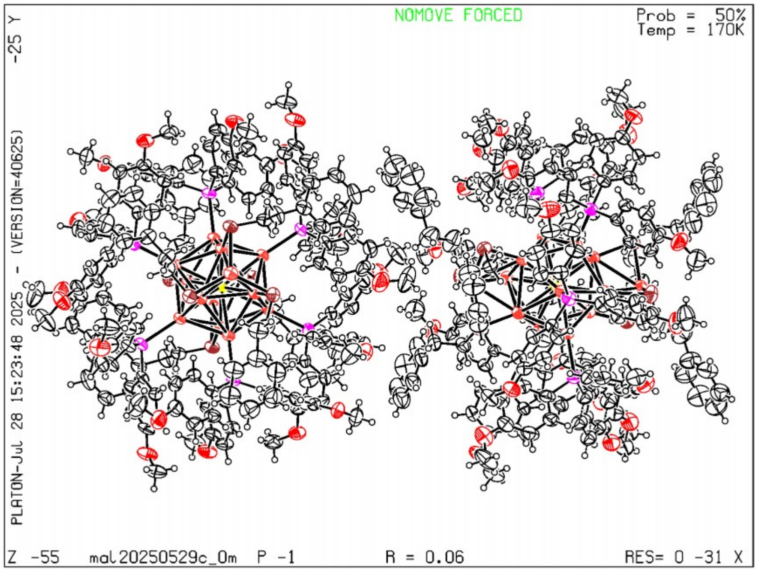

Fig. S3 The thermal ellipsoids of the ORTEP diagram of the **Pt_1Ag_{14}-2** NC.

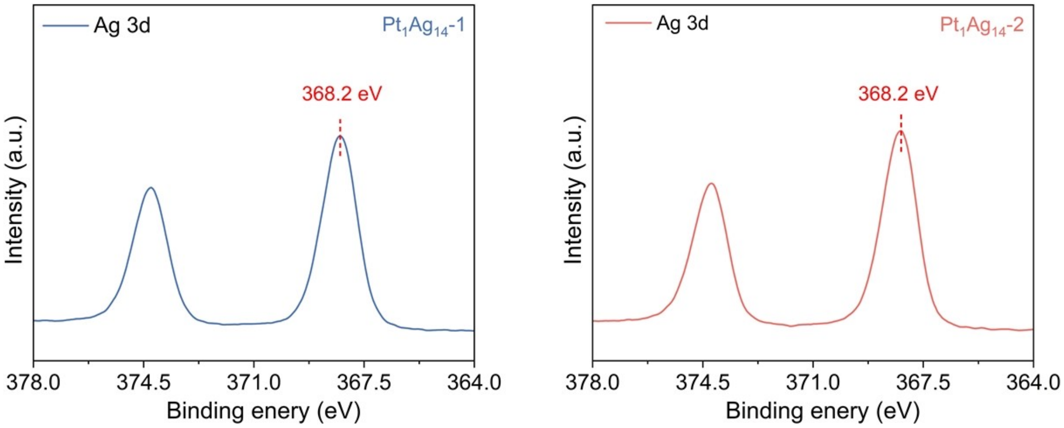

Fig. S4 Ag 3d spectra of **Pt_1Ag_{14}-1** (blue) and **Pt_1Ag_{14}-2** (red) NCs.

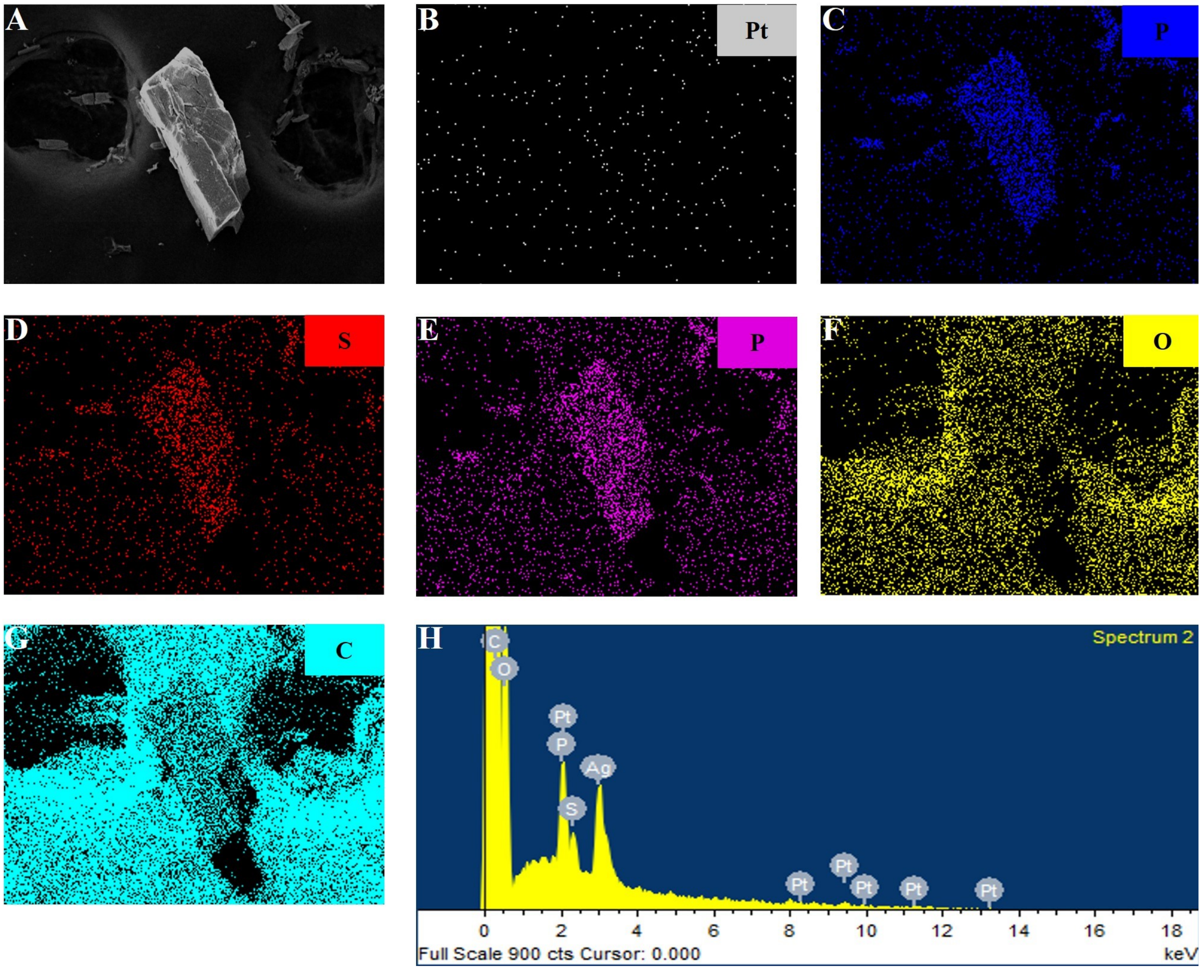

Fig. S5 SEM image and corresponding elemental mapping images of the **Pt_1Ag_{14}-1** crystals. (A) SEM image of single crystal; (B)-(G) Elemental mapping images of Pt, Ag, S, P, O, and C elements, respectively; (H) EDS spectrum confirming the presence of above elements (Pt, Ag, S, P, O, and C) in **Pt_1Ag_{14}-1** NC.

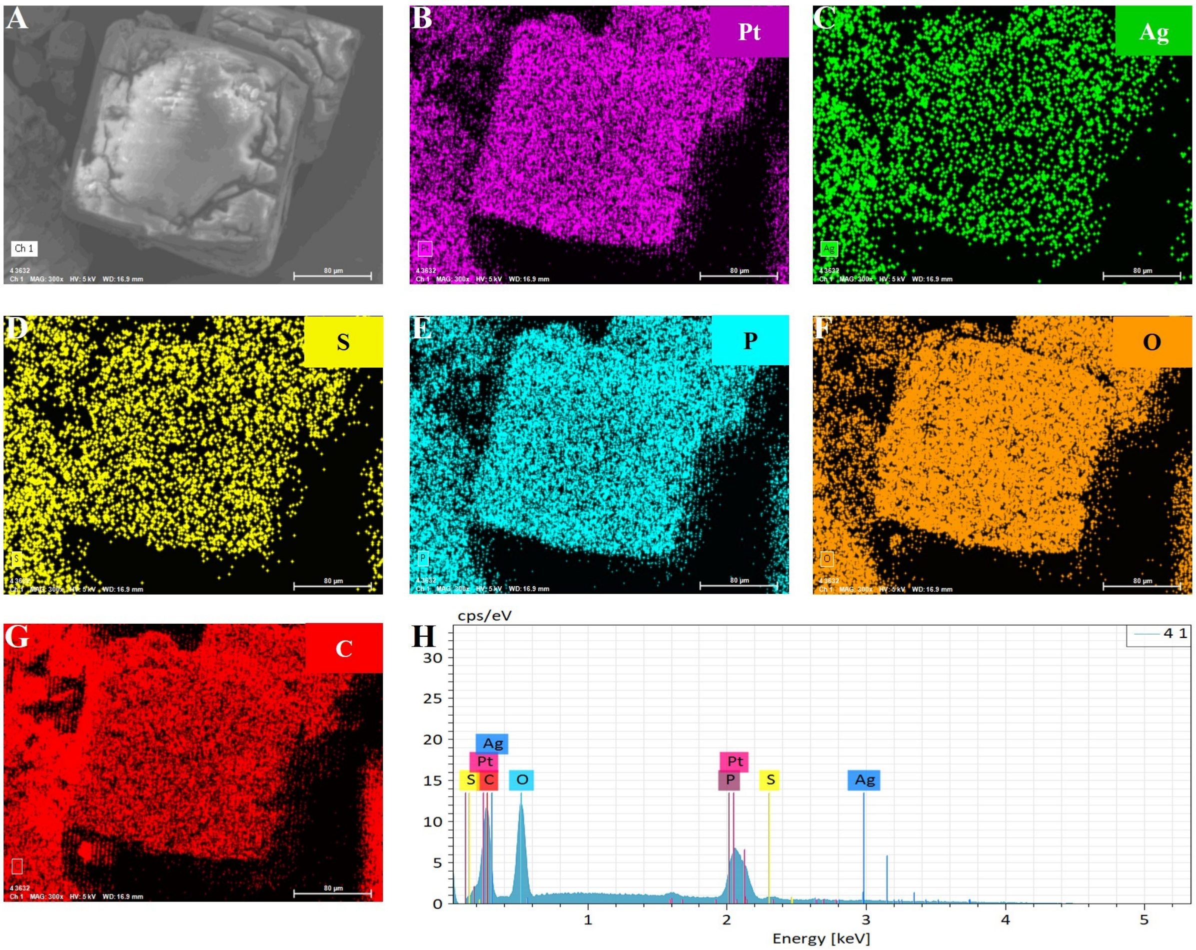

Fig. S6 SEM image and corresponding elemental mapping images of the **Pt$_1$Ag$_{14}$-2** crystals. (A) SEM image of single crystal; (B)-(G) Elemental mapping images of Pt, Ag, S, P, O, and C elements, respectively; (H) EDS spectrum confirming the presence of above elements (Pt, Ag, S, P, O, and C) in **Pt$_1$Ag$_{14}$-2** NC.

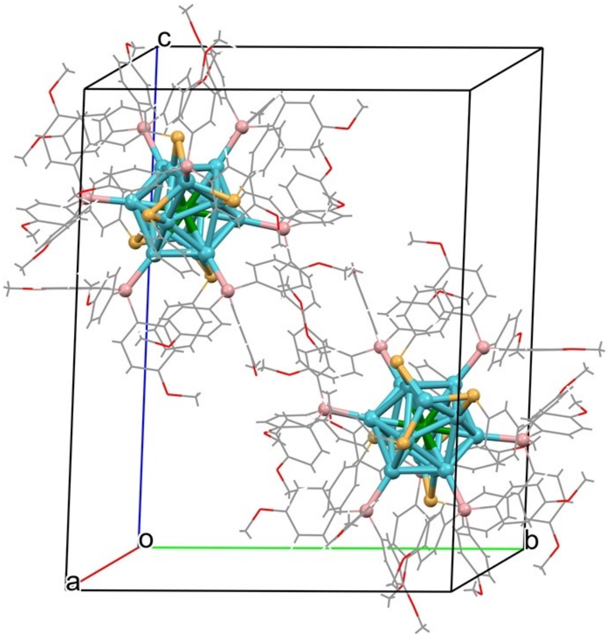

Fig. S7 The presence of two $\mathbf{Pt_1Ag_{14}}$**-1** NC molecules in a unit cell. Color labels: green = Pt; turquoise = Ag; gold = S; pink = P; red = O; grey = C; white = H.

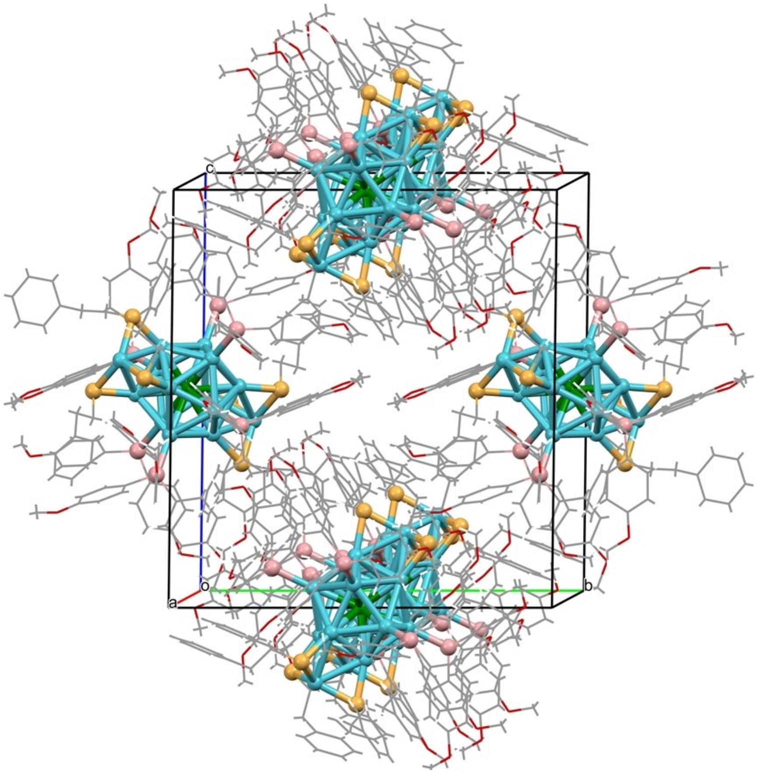

Fig. S8 The presence of six $\mathbf{Pt_1Ag_{14}}$**-2** NC molecules in a unit cell. Color labels: green = Pt; turquoise = Ag; gold = S; pink = P; red = O; grey = C; white = H.

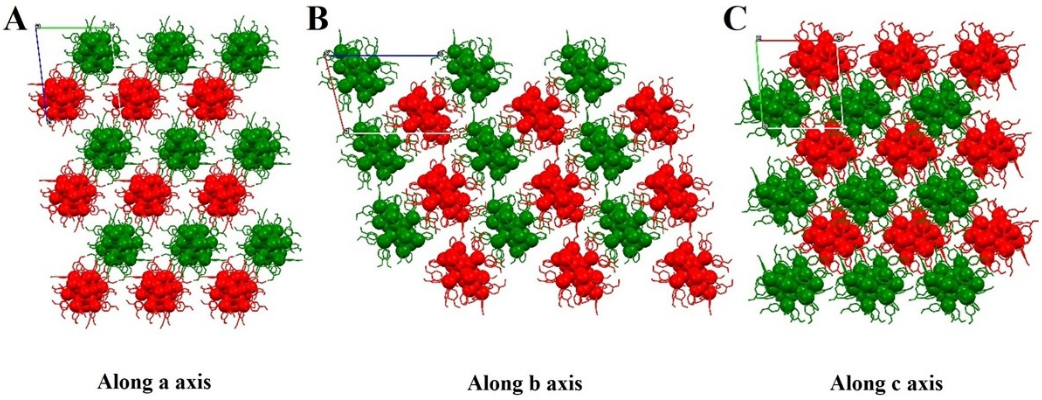

Fig. S9 Packing mode of **Pt_1Ag_{14}-1** in the crystal shown. (A) Along the a axis; (b) along the b axis; (c) along the c axis. All H atoms are omitted for clarity. The cluster molecules arranged in different directions show in different colors.

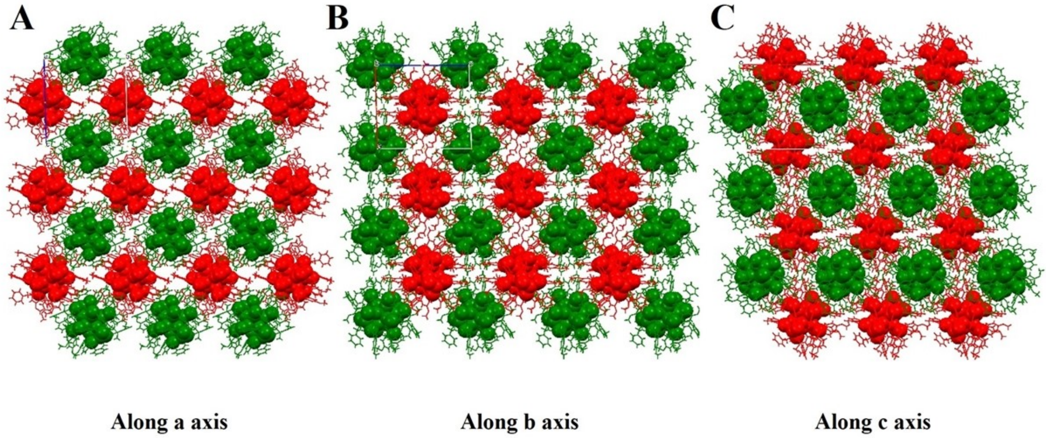

Fig. S10 Packing mode of **Pt_1Ag_{14}-2** in the crystal shown. (A) Along the a axis; (b) along the b axis; (c) along the c axis. All H atoms are omitted for clarity. The cluster molecules arranged in different directions show in different colors.

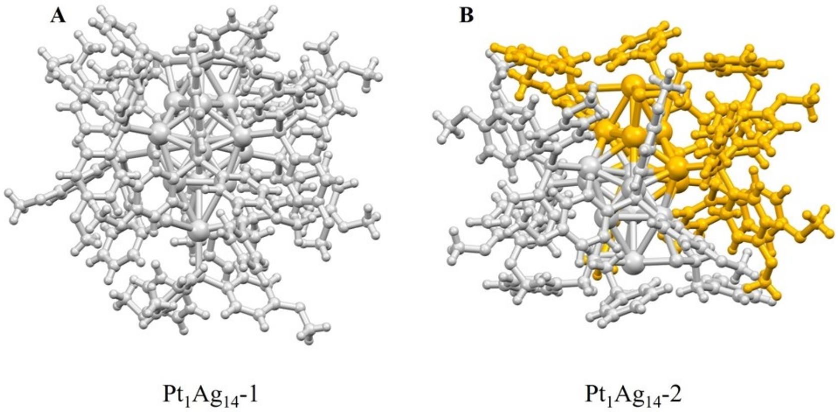

Fig. S11 Comparison of the molecular symmetry between **Pt$_1$Ag$_{14}$-1** and **Pt$_1$Ag$_{14}$-2** clusters. (A) **Pt$_1$Ag$_{14}$-1**; (B) **Pt$_1$Ag$_{14}$-2**.

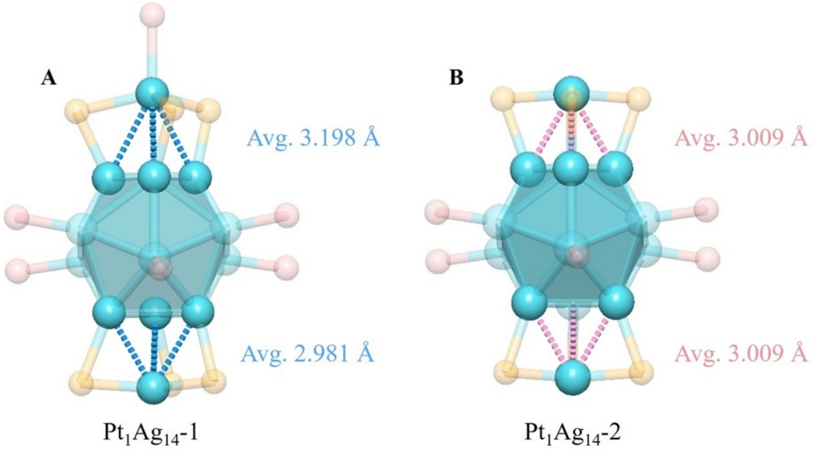

Fig. S12 The change in the distance between the shell Ag and the icosahedral surface Ag. Color labels: green = Pt; turquoise = Ag; gold = S; pink = P.

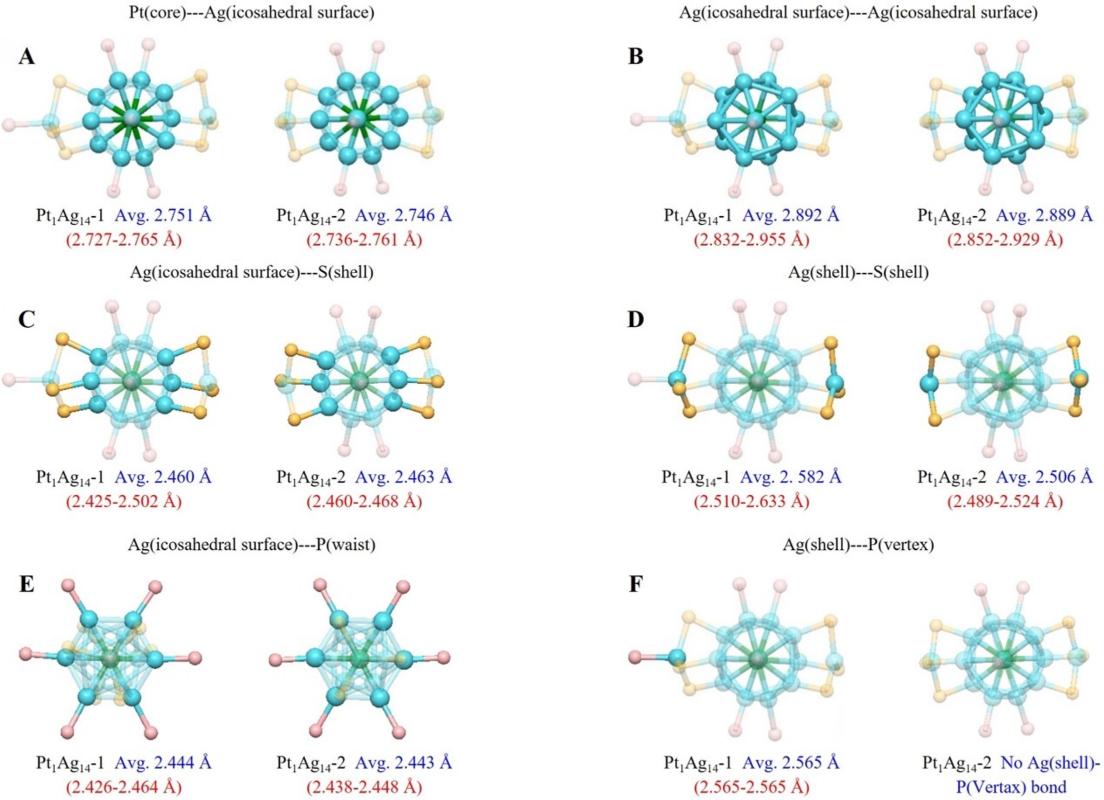
Pt(core)---Ag(icosahedral surface)

Ag(icosahedral surface)---Ag(icosahedral surface)

Ag(icosahedral surface)---S(shell)

Ag(shell)---S(shell)

Ag(icosahedral surface)---P(waist)

Ag(shell)---P(vertex)

Fig. S13 Structural comparison and bond length among **Pt_1Ag_{14}-1**, and **Pt_1Ag_{14}-2** NCs. (A) Comparison of the bond length of Pt(core)---Ag(icosahedral surface); (B) Comparison of the bond length of Ag(icosahedral surface)---Ag(icosahedral surface); (C) Comparison of the bond length of Ag(icosahedral surface)---S(shell); (D) Comparison of the bond length of Ag(shell)---S(shell); (E) Comparison of the bond length of Ag(icosahedral surface)---P(waist); (F) Comparison of the bond length of Ag(shell)---P(shell). Color labels: green = Pt; turquoise = Ag; gold = S; pink = P.

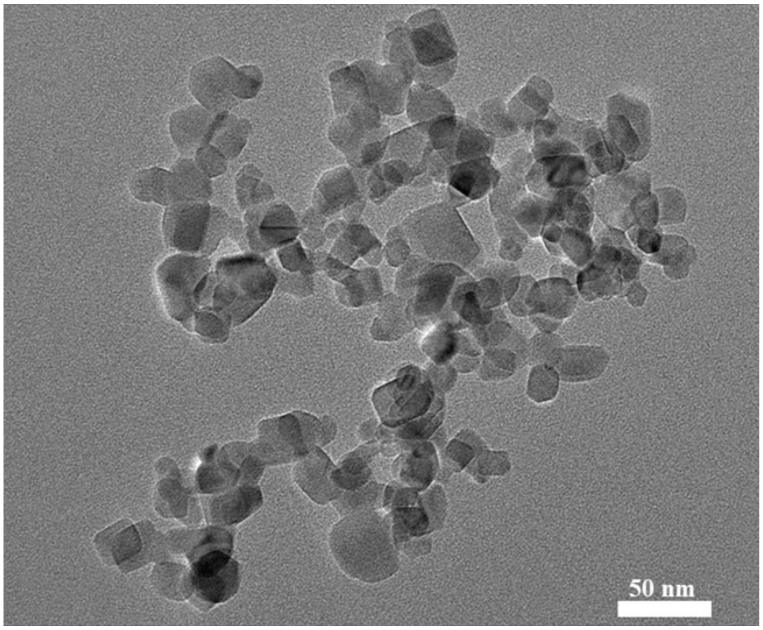

Fig. S14 TEM image of $\mathbf{TiO_2}$ nanoparticles.

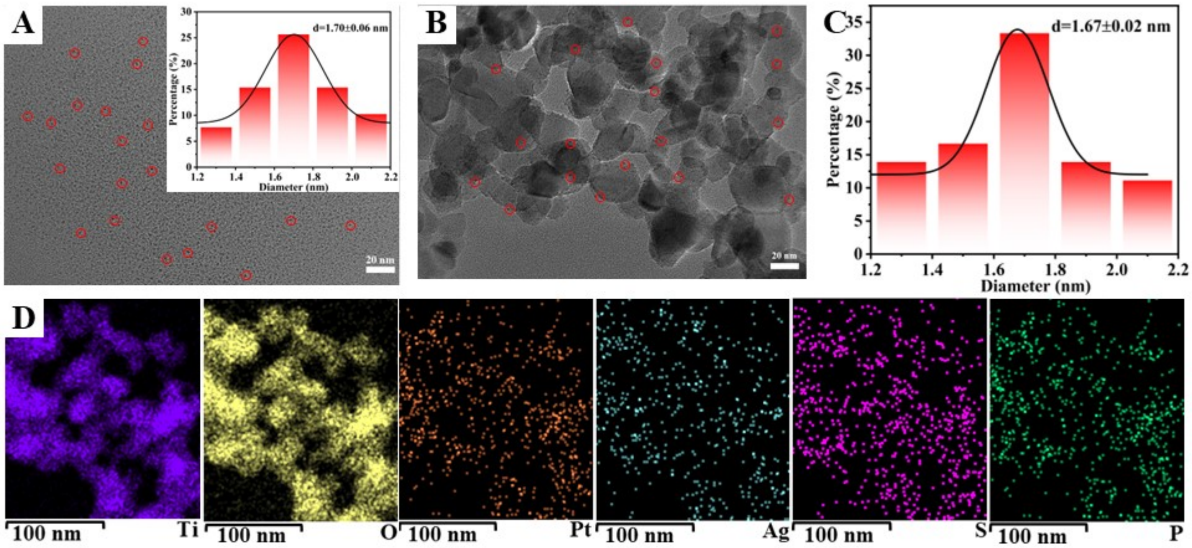

Fig. S15 TEM and elemental mapping analyses of $\mathbf{Pt_1Ag_{14}}$**-2** and $\mathbf{Pt_1Ag_{14}}$**-2/**$\mathbf{TiO_2}$ composites. (A) TEM image and size distribution histogram (inset) of the unsupported $\mathbf{Pt_1Ag_{14}}$**-2** NCs. (B) TEM image of $\mathbf{Pt_1Ag_{14}}$**-2/**$\mathbf{TiO_2}$. (C) Size distribution histogram of the clusters obtained from the image in panel (B). (D) Corresponding EDX elemental mappings for Ti, O, Pt, Ag, S, and P in $\mathbf{Pt_1Ag_{14}}$**-2/**$\mathbf{TiO_2}$.

Additional discussion:

Transmission electron microscopy (TEM) and elemental mapping verified that $\mathbf{Pt_1Ag_{14}}$ NCs are uniformly dispersed on the TiO_2 support without obvious aggregation.

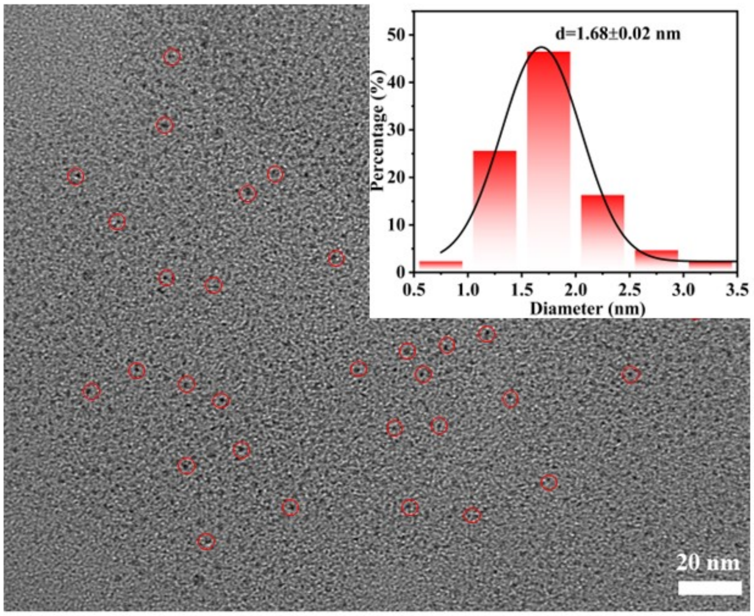

Fig. S16 TEM image and size distribution histogram (inset) of the unsupported **Pt_1Ag_{14}-1** NCs.

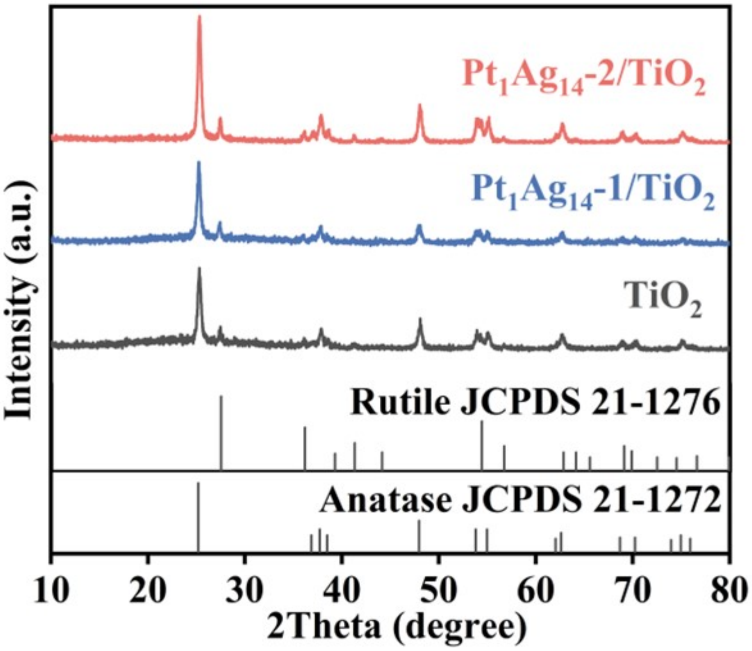

Fig. S17 Powder XRD patterns of **TiO_2**, **Pt_1Ag_{14}-1/TiO_2, and Pt_1Ag_{14}-2/TiO_2**.

Additional discussion:

As shown in Fig. S17, both the **Pt_1Ag_{14}-1/TiO_2** and **Pt_1Ag_{14}-2/TiO_2** samples displayed a mixed TiO_2 crystal phase, and the cluster loading process did not induce any structural alterations to the TiO_2 framework.

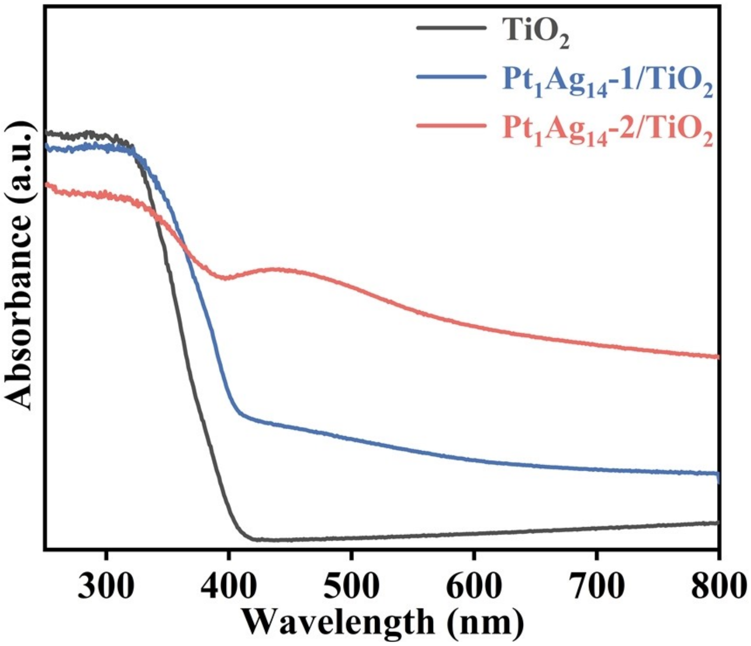

Fig. S18 UV-vis diffuse reflection spectroscopy of **TiO_2**, **Pt_1Ag_{14}-1/TiO_2**, and **Pt_1Ag_{14}-2/TiO_2**.

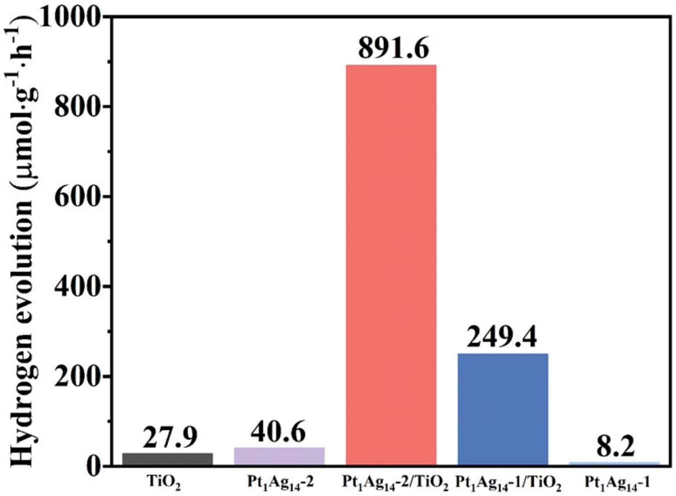

Fig. S19 Hydrogen generation rates of pristine **TiO_2**, **Pt_1Ag_{14}-1** NCs, **Pt_1Ag_{14}-2** NCs, **Pt_1Ag_{14}-1/TiO_2** and **Pt_1Ag_{14}-2/TiO_2** composite.

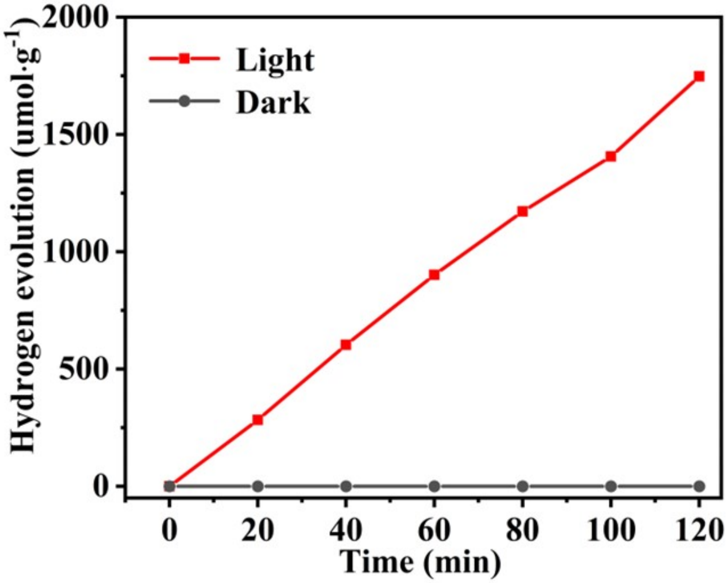

Fig. S20 Photocatalytic H_2 production performance of **Pt_1Ag_{14}-2/TiO_2** under alternating light on and off conditions.

Additional discussion:

In light-dark control tests, no H_2 was detected in the dark, indicating that illumination is essential and excluding side reactions between the nanoclusters and the sacrificial agent.

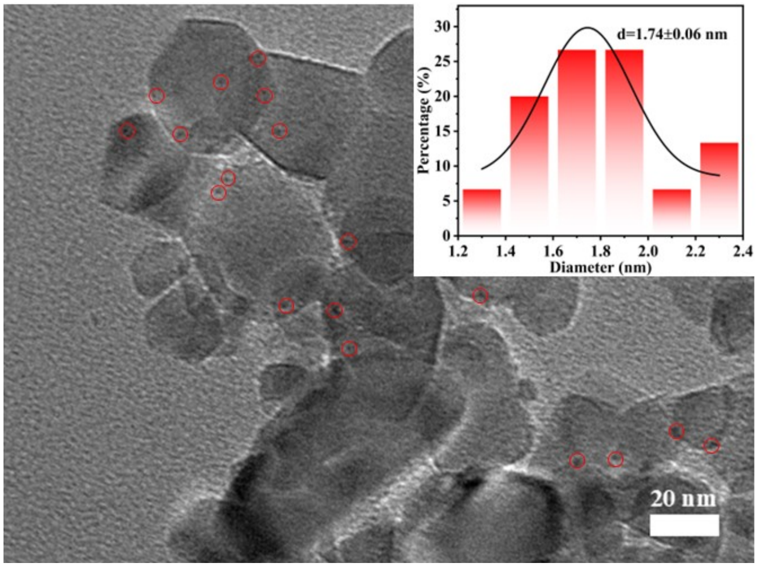

Fig. S21 HRTEM images and size distribution histogram of **Pt_1Ag_{14}-2** NCs in **Pt_1Ag_{14}-2/TiO_2** after the photocatalytic reaction.

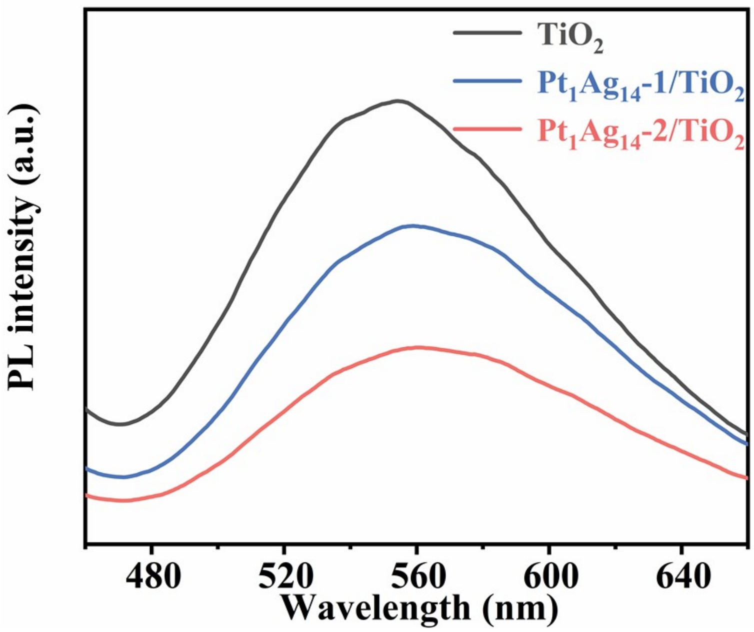

Fig. S22 Photoluminescence spectra obtained with 365 nm excitation for **TiO$_2$**, **Pt$_1$Ag$_{14}$-1/TiO$_2$** and **Pt$_1$Ag$_{14}$-2/TiO$_2$**.

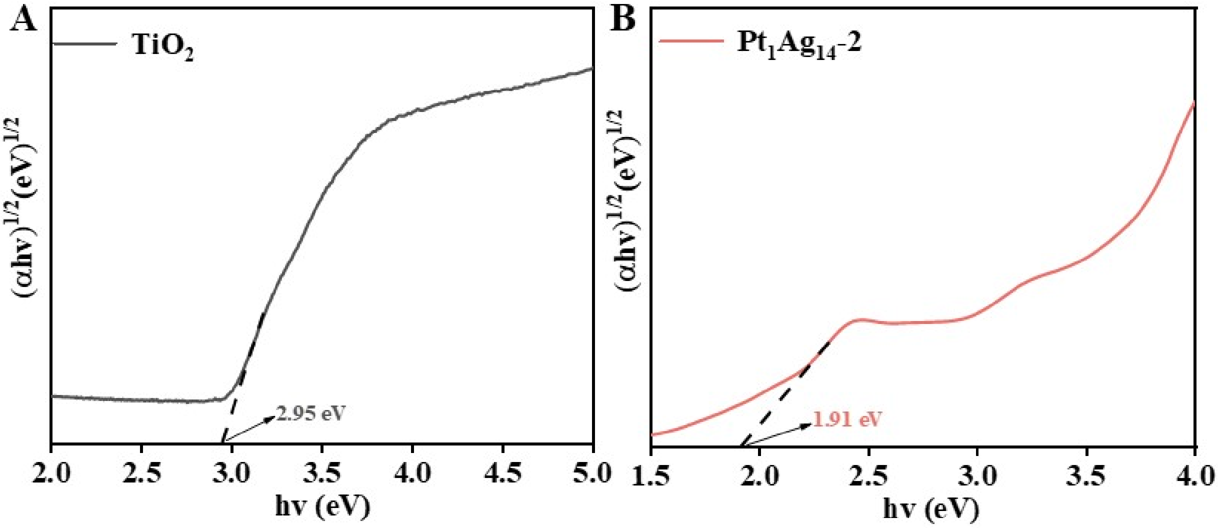

Fig. S23 Tauc plots of (A) **TiO$_2$**, and (B) **Pt$_1$Ag$_{14}$-2**.

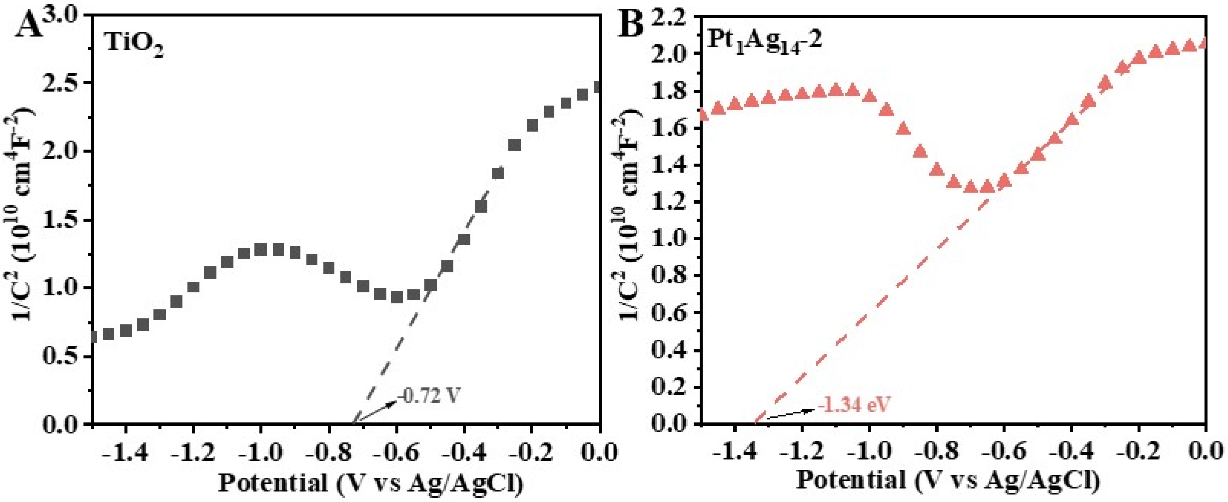

Fig. S24 Mott-Schottky plots of (A) **TiO$_2$**, and (B) **Pt$_1$Ag$_{14}$-2** frequencies of 5000 Hz.

Additional discussion:

The bandgap is determined by the Kubelka-Munk formula.

$$(\alpha h v)^{1/2} = A\left(hv - E_g\right)\#(1)$$

In this equation, α denotes the absorption coefficient, A is a constant, h is Planck's constant, and ν is the frequency. The bandgap energy (Eg) was derived from a Tauc plot of $(\alpha h\nu)^{1/2}$ against hν, obtained by extrapolating the linear segment of the plot to find its intercept on the hν axis.

The band edge positions of photocatalysis can be calculated using the following equation:

$$E_{CB} = (V\ vs\ NHE) = E_{fb}\,(V\ vs\ AgCl/Ag) + 0.197 - X\#(2)$$

$$E_{VB} = E_{CB} + E_g\#(3)$$

Here, E_{VB} and E_{CB} denote the valence band and conduction band edge potentials, respectively. $E_{Ag/AgCl}$ is 0.197 V versus NHE in a saturated KCl solution, and X represents the voltage difference between the conduction band and the flat band potential. For an n-type semiconductor, the flat band potential E_{fb} is typically approximately equivalent to E_{CB}.

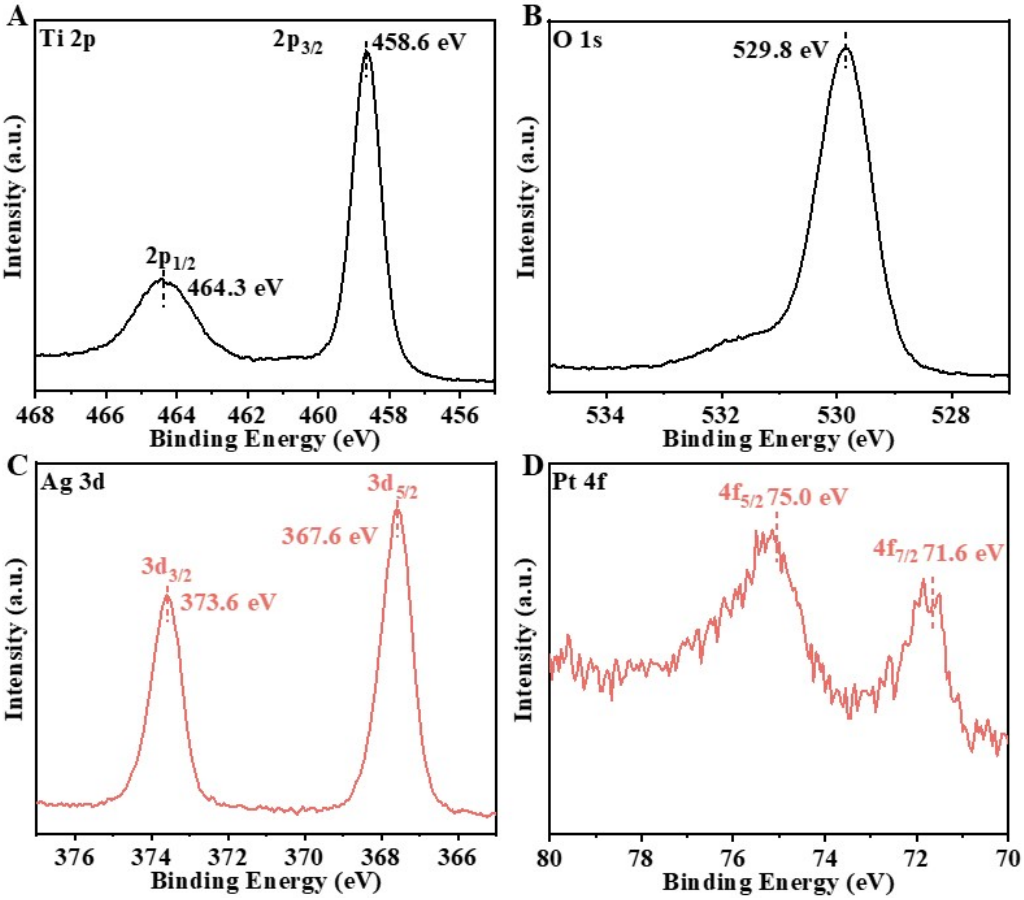

Fig. S25 XPS spectra of (A) Ti 2p, (B) O 1s (C) Ag 3d and (D) Pt 4f for **Pt_1Ag_{14}-2/TiO_2**.

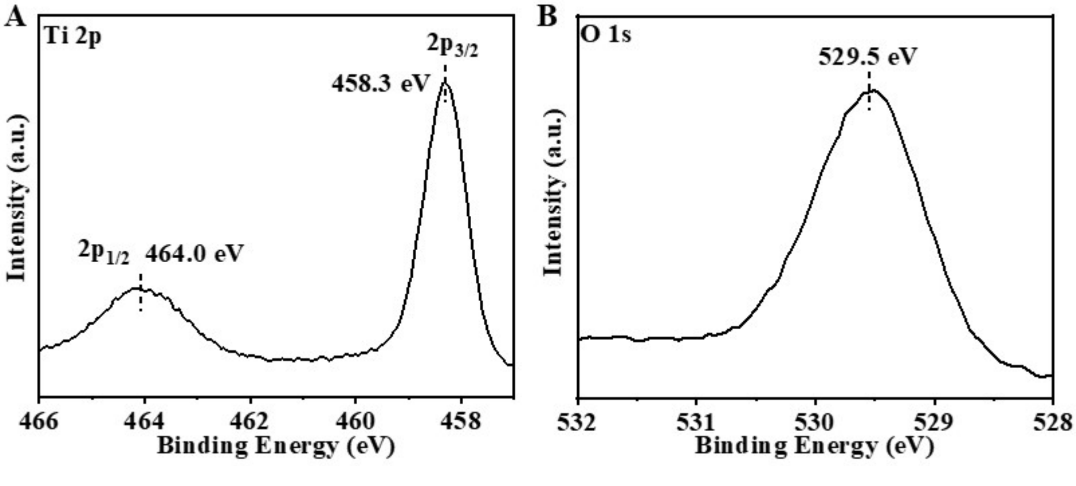

Fig. S26 XPS spectra of (A) Ti 2p and (B) O 1s for **TiO_2**.

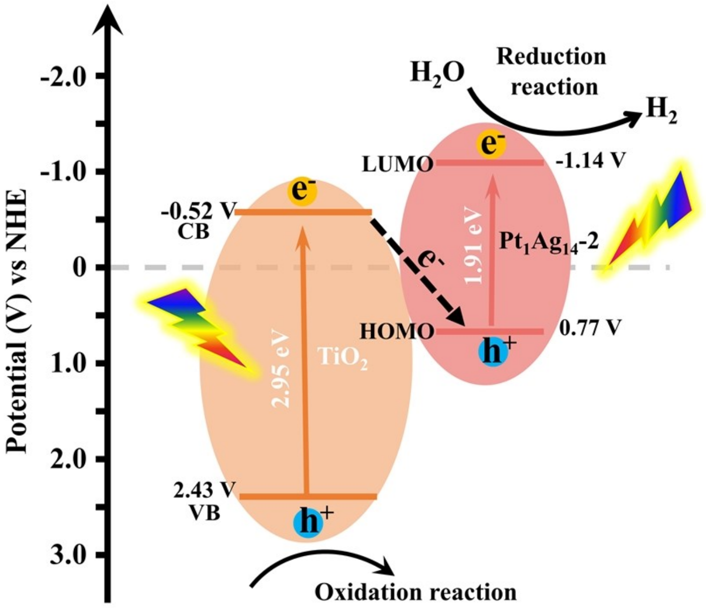

Fig. S27 Schematic of the energy level diagram and the mechanism of photocatalytic H_2 generation under solar irradiation in **Pt_1Ag_{14}-2/TiO_2** photocatalysts.

Additional discussion:

Upon solar irradiation, electrons in **TiO_2** are excited from the valence band (VB) to the conduction band (CB), while electrons in the **Pt_1Ag_{14}-2** NCs are promoted from the HOMO to the LUMO. The photogenerated holes left behind in the **TiO_2** VB (+2.43 V vs. NHE at pH=7) possess sufficient oxidative potential for water oxidation. Meanwhile, the photoexcited electrons in **TiO_2** rapidly transfer to the HOMO of the clusters. Electrons on the LUMO of the clusters are then utilized to reduce protons for H_2 generation. This interfacial charge-transfer pathway constitutes a direct Z-scheme heterojunction, effectively maximizing redox potentials for photocatalytic hydrogen production in the **Pt_1Ag_{14}-2/TiO_2** system.

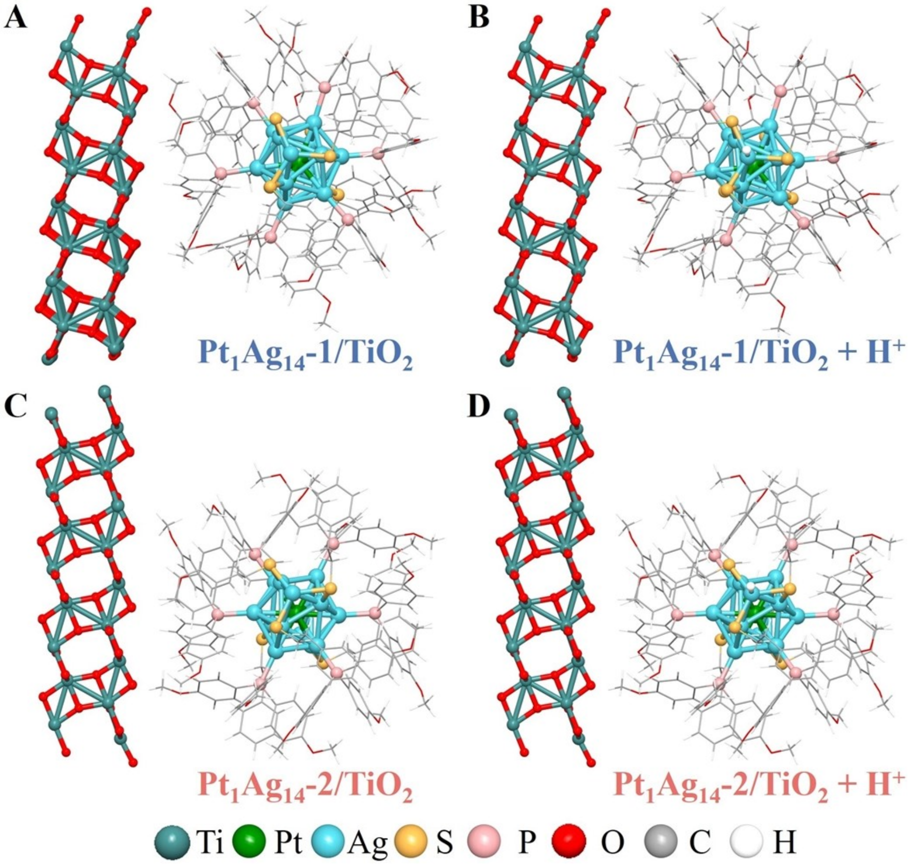

Fig. S28 Comparison of the atomic models before and after H^+ adsorption: (A) and (C) show the original structures of **Pt_1Ag_{14}-1/TiO_2** and **Pt_1Ag_{14}-2/TiO_2**, respectively; (B) and (D) present the corresponding structures after H^+ adsorption.

Section 3. Supporting Table

Table S1 Crystal data and structure refinement for **Pt_1Ag_{14}-2**.

Empirical formula	$C_{174}H_{180}Ag_{14}O_{18}P_6PtS_6$
Formula weight	4642.62
Temperature/K	170
Crystal system	triclinic
Space group	$P\bar{1}$
a/Å	19.759(6)
b/Å	20.696(6)
c/Å	22.251(7)
α/°	88.498(5)
β/°	88.172(5)
γ/°	84.406(6)
Volume/Å^3	9049(5)
Z	2
ρ_{calc}g/cm^3	1.704
μ/mm^{-1}	2.427
F(000)	4580.0
Crystal size/mm^3	0.2 × 0.18 × 0.09
Radiation	Mo Kα (λ = 0.71073)
2Θ range for data collection/°	3.956 to 50.5
Index ranges	$-23 \leq h \leq 23$, $-24 \leq k \leq 24$, $-26 \leq l \leq 26$
Reflections collected	186655
Independent reflections	32763 [R_{int} = 0.0621, R_{sigma} = 0.0492]
Data/restraints/parameters	32763/592/1959
Goodness-of-fit on F^2	1.083
Final R indexes [I>=2σ (I)]	R_1 = 0.0583, wR_2 = 0.1347
Final R indexes [all data]	R_1 = 0.0948, wR_2 = 0.1491
Largest diff. peak/hole / e Å^{-3}	2.56/−1.70